Down-looking synthetic aperture imaging ladar demonstrator and its experiments over 1.2 km outdoor

Zhu Luan (栾 竹)[*], **Jianfeng Sun (孙建锋), Yu Zhou (周 煜), Lijuan Wang (王利娟),**
Mei Yang (杨 媚), and Liren Liu (刘立人)

Key Laboratory of Space Laser Communication and Detection Technology,
Institute of Optics and Fine Mechanics, Chinese Academy of Sciences,
Shanghai 201800, China
[*]*Corresponding author: luanzhu@siom.ac.cn*

We present a down-looking synthetic aperture imaging ladar demonstrator and its experiments over 1.2 km in the field. The achieved imaging resolution is in agreement with the theoretical design, and the resulting two-dimensional image is satisfied. The capability to eliminate the influence from atmospheric turbulence is fully proven by the experiments.

OCIS codes: 100.2000, 100.3010, 110.0110, 280.6730.
doi: 10.3788/COL201412.111101.

A synthetic aperture imaging ladar (SAIL) which necessarily works in a side-looking mode can provide fine resolution, two-dimensional (2D) active imaging at a long range. It recently became an interesting field of research, and a number of laboratory experiments and a flight demonstration of side-looking SAILs were reported[1–5]. However, a narrow footprint is inherent to side-looking SAILs, and similarly due to the directivity of heterodyne detection, the optical aperture of receiving optics is restricted to one of the transmitting optics, which are both limited unacceptably within a very small size. Also a matched optical delay line must be used to guarantee the beat frequencies from heterodyne to a reasonable range. Moreover, the phase interferences from atmospheric turbulence and mechanical trembling in environments will seriously affect and even destroy the imaging.

Based on the projection imaging of spatial phase distributions from SAIL to target, we propose a concept of down-looking SAIL[6,7] with a transmitter of two coaxial and scanned polarization-orthogonal beams of spatial spherical and parabolic phase difference, and a receiver of self-heterodyne detection. Therefore, the implementation employs synthetic aperture imaging using quadratic phase history reconstruction in the travel direction similar to side-looking SAIL and linear phase modulation reconstruction in the orthogonal direction of travel analogous to side-looking SAIL. The down-looking SAIL achieves fine-resolution and long-distance 2D imaging with relaxed aperture size, and thus has its natural feature that the size of optical footprint together with their associated imaging resolution is controllable and changeable in a large scale. Consequently, the footprint width can be enhanced, the receiving aperture can be intensely increased, the influence from atmospheric turbulence and unmodeled line-of-sight motion can be automatically compensated, and in principle,

no optical delay is needed. However, the algorithm for image reconstruction in the down-looking SAIL is the same as that in the side-looking SAIL. It is also seen that for side-looking SAIL the range resolution is along the line-of-sight direction, whereas for down-looking SAIL the range resolution is in the lateral direction on the target plane.

Down-looking SAIL significantly relaxes the difficulties in side-looking SAIL. Obviously, down-looking SAIL provides a possibility to move this 2D imaging technique into practical use. In this letter, a down-looking SAIL demonstrator and its experimental imaging results over 1.2 km outdoor range under the influence of strong atmospheric turbulence are provided, which shows a progress of the demonstrator before verification with an optical collimator in the laboratory[8].

Figure 1 shows the principle structure of the demonstrator The transmitter consists of a laser, a polarization modification of Mach–Zehnder (M-Z) interferometer, and a transmitting lens. The M-Z device is used to split the input laser beam into two beams and then to combine them into one. The left arm consists of a window, a closely placed x-directed cylindrical lens L_1, and a y-directed cylindrical lens L_2, and the right arm consists of a window and an x-directed cylindrical lens L_3, as depicted in Fig. 1. L_2 is used to generate spatial quadratic phase in the travel direction, and the shift of L_1 and L_3 is to produce linear phase modulation in the orthogonal direction of travel. It is be noted that this M-Z device has two specially designed polarization beam splitting combinations of a polarization beam splitter (PBS), a $\lambda/4$ wave plate (WP), and a mirror. In combinations, the parallel polarization component passes through the PBS directly and the vertical polarization component via the WP and the mirror is rotated in polarization by 90° and crosses the PBS. It can be understood that this combination delays the vertical
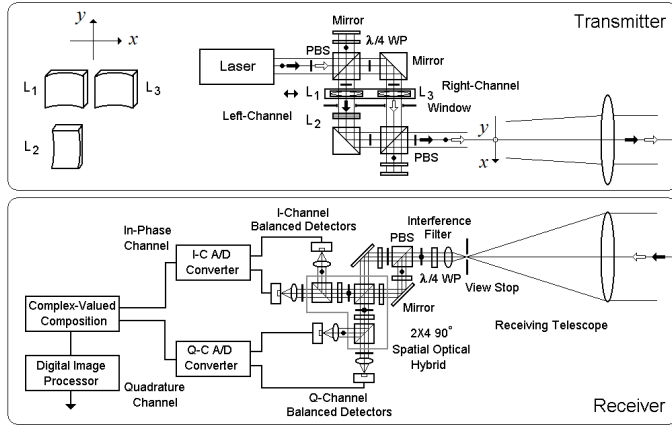
Fig. 1. Structure of down-looking SAIL demonstrator.

polarization component and furthermore reverses its optical field, so that the focus of the transmitting lens can exactly locate on the two windows on the same plane. The joint shift of L_1 and L_3 derived by a linear motor results in a countermove of their phase distributions in the output of the M-Z device. The transmitting lens projects and images the optical fields near the windows onto the target plane with an amplification factor of $M = Z/f_t$ [7]. The receiver consists of a receiving telescope, a 2×4 90° spatial optical hybrid, and a digital imaging processor, which is similar to our previous work[7,9]. The phase difference between the orthogonally polarized fields received from a target can thus be converted to a complex expression. In an alternative way, we can use only a balanced detection of hybrid in the receiver together with a bias of pre-arranged shift between L_1 and L_3 in the transmitter[10]. The built demonstrator is shown in Fig. 2. The optical fields in the left and right channels on the window plane in the M-Z device can be described, respectively, by

$$e_\mathrm{L}(x,y:t_\mathrm{f}) = E_t\mathrm{rect}\left(\frac{t_\mathrm{f}}{\Delta T}\right)\mathrm{rect}\left(\frac{x}{W_x}\right)\mathrm{rect}\left(\frac{y}{W_y}\right)$$
$$\exp\left[\mathrm{j}\frac{\pi}{\lambda f'_x}(x+v_x t_\mathrm{f})^2\right]\exp\left[\mathrm{j}\frac{\pi}{\lambda f'_y}y^2\right],$$

$$e_\mathrm{R}(x,y:t_\mathrm{f}) = E_t\mathrm{rect}\left(\frac{t_\mathrm{f}}{\Delta T}\right)\mathrm{rect}\left(\frac{x}{W_x}\right)\mathrm{rect}\left(\frac{y}{W_y}\right)$$
$$\exp\left[\mathrm{j}\frac{\pi}{\lambda f'_x}(x-v_x t_\mathrm{f})^2\right], \tag{1}$$

where t_f is the fast time for each shifting, ΔT the time width of shift, W_x and W_y are the window sizes, f'_x is the equivalent curvature radius of L_1 and L_3 on the window plane, f'_y is the equivalent curvature radius of L_2, and v_x is the shifting speed of L_1 and L_3.

For a point target of $(x_\mathrm{p}, y_\mathrm{p})$, the 2D data collection equation related to the complex current output is given by

$$i(x_\mathrm{p},y_\mathrm{p}:t_\mathrm{f},n) = K\mathrm{rect}\left(\frac{t_\mathrm{f}}{\Delta T}\right)\mathrm{rect}\left(\frac{x_\mathrm{p}}{D_x}\right)\mathrm{rect}\left(\frac{y_\mathrm{p}-nd_s}{D_y}\right)$$
$$\exp\left[\mathrm{j}\frac{\pi}{\lambda f_x/2}2x_\mathrm{p}v_x t_\mathrm{f} + \mathrm{j}\frac{\pi}{\lambda f_y}(y_\mathrm{p}-nd_s)^2\right], \tag{2}$$

where d_s is the sampling step along SAIL moving, n is the sampling index, $D_x = MW_x$ and $D_y = MW_y$ are the illumination sizes on target, $f_x = M^2 f'_x$ and $f_y = M^2 f'_y$ are the curvature radii of the corresponding spatial phases on the target plane, and K includes all the factors of transmission, propagation, and optical-to-electrical conversion. Typically, the imaging in the orthogonal direction of travel is focused in terms of Fourier transform, whereas the imaging in the travel direction uses the match filter operation with a conjugation of the phase history[7].

A frequency-doubled Nd:YAG CW laser of 532 nm wavelength with single-frequency of 5 MHz linewidth, and 0.25–5 W output power is used. The transmitting lens has the focal length of 1.2 m and the aperture diameter
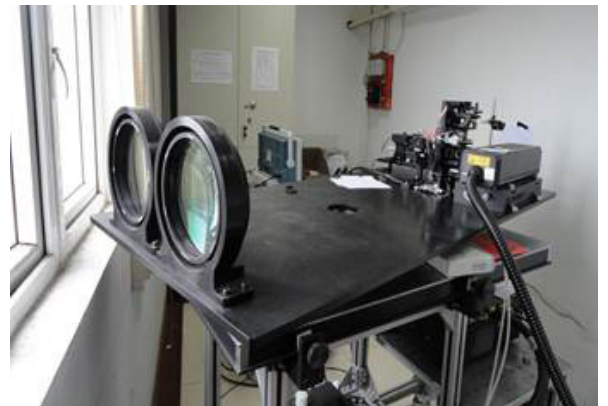

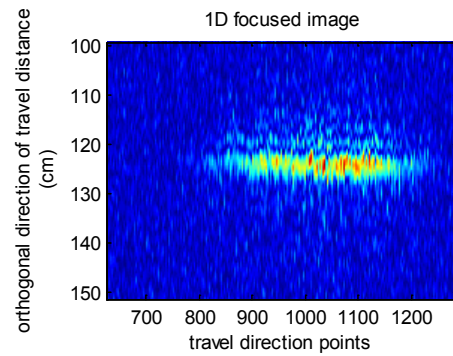Fig. 2. Open view of built down-looking SAIL demonstrator.

of 200 mm. L_1, L_2, and L_3 are negative cylindrical lenses and the focal lengths are all 60 mm. L_1 and L_3 are located 30 mm behind the focal plane of the transmitting lens, and the distance between L_1 and L_2 is 10 mm. The repeated frequency of shifting of L_1 and L_3 is 4 Hz. The beam diameter, that is, the window diameter is 2 mm, which corresponds to a 1 s time duration of shifting, but the adapted time in the Fourier transform is 0.8 s. The amplification factor of receiving telescope is 25×, and the main lens has the focal length of 1.2 m and the aperture diameter of 200 mm. Owing to the narrow sensitive size of photodetectors, the receiving view field is about 1 mrad. To simulate the SAIL moving, a rotatable platform is utilized with the angular scanning speed of 10.5 μrad/s, which greatly relaxes the requirement for data sampling. From the design, the theoretical imaging resolutions in full-width at half-height (FWHH) are estimated as $d_x \times d_y = 3.1 \times 4.5$ (cm) for a point target and about $d_x \times d_y = 4.6 \times 6$ (cm) for a 3×3 (cm) target.

The experiments are so arranged that the demonstrator and the target are located, respectively, at the 4th floor and the 13th floor of two buildings, and the distance between them is 1.2 km. Figure 3 shows the perspective of the building to fix the target, which was taken during one experiment.
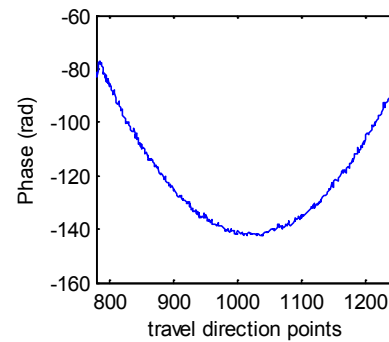
The optical path goes across two busy highways and a restaurant, and thus suffers from strong atmospheric turbulence. The first experiment evaluates the practical image resolution of the demonstrator by using a square 3×3 (cm) target cut from retro-reflective tape and a 2.5 W laser power is used. The magnitude and the phase distributions of the focused image in the orthogonal direction of travel via the Fourier transform are shown in Figs. 4(a) and (b). From Figs. 4(a) and (b), the final image resulting from the next focusing in the travel direction via match filtering is as shown in Fig. 4(c). The FWHH resolutions are measured as
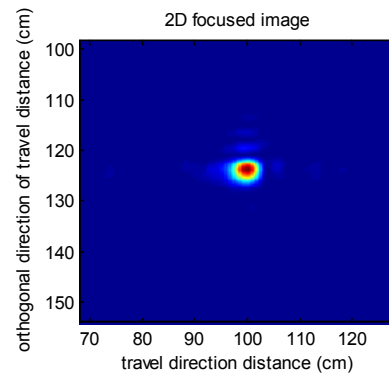

(a)

(b)

(c)

Fig. 4. (a) Magnitude and (b) phase distributions of focused image in the orthogonal direction of travel and (c) 2D image focused subsequently in the travel direction for a 3×3 (cm) point target.
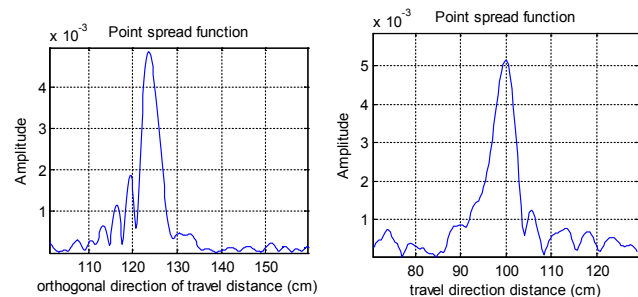

Fig. 3. Photograph of building to fix target and the arrow indicates the position of target.

Fig. 5. Point spread functions in the orthogonal direction of travel and in the travel direction.
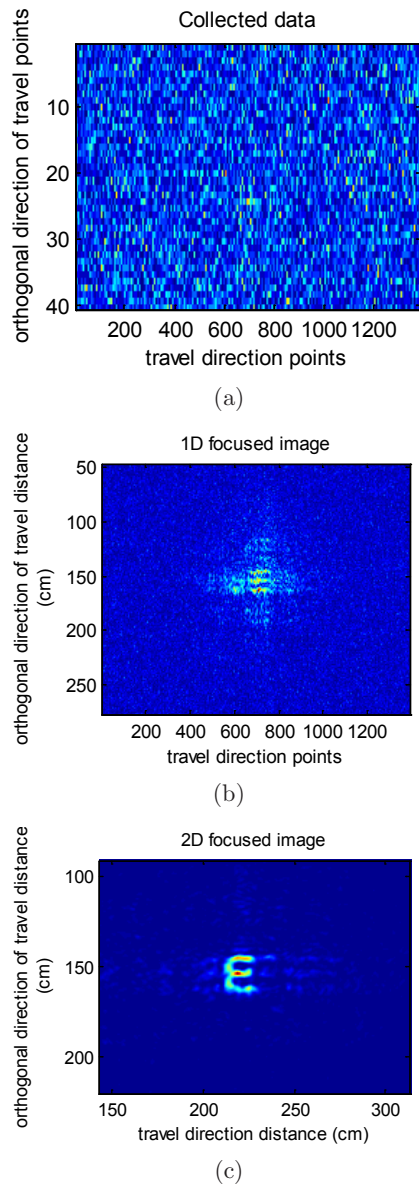
(a)

(b)

(c)

Fig. 6. (a) Collected data of the target "*E*". (b) Focused image in the orthogonal direction of travel. (c) Resulting image after next focusing in the travel direction.

$d_x \times d_y = 5.5 \times 6.8$ (cm), as shown in Fig. 5. The deviation from the theoretical calculation is considered in the orthogonal direction of travel mostly from the nonlinearity of lens shifting and in the travel direction mainly owing to the changed aperture-synthesizing length from the center of the circular footprint.

The target then tested is a letter "*E*" of the size 15×24 (cm) cut from retro-reflective tape. The collected 2D data, the focused image in the orthogonal direction of travel, and the final image subsequently focused in the travel direction are shown in Figs. 6(a), (b), and (c), respectively. From the theoretical point[6,7] the ideal point spread function approaches the sinc function, which has sidelobes of periodical distribution. Therefore, the sidelobe-like shadows appear near the focused image as shown in Figs. 4(a) and (c) and 5(b) and (c). This phenomenon is similar to that caused by the Airy disc in imaging by a lens. As predicted[7,11], the laser speckle effect is observed on the resulting image of the target.

It should be emphasized that almost all experiments in day or night were successful under various atmospheric conditions. The refractive-index structure parameter C_n^2 measured at most time was worse than 10^{-15} m$^{-2/3}$.

In conclusion, we present a down-looking SAIL demonstrator and its imaging experiments over 1.2 km distance in the field. The achieved imaging resolution is 5.5×6.8 (cm) near the design and resulting 2D image is satisfied. The capability of down-looking SAIL to eliminate the influence from atmospheric turbulence and other phase interference is verified by the experiments, which promises that this kind of down-looking SAIL is of great potential for practical application.

References

1. M. Bashkansky, R. L. Lucke, E. Funk, L. J. Rickard, and J. Reintjes, Opt. Lett. **27,** 1983 (2002).
2. S. M. Beck, J. R. Buck, W. F. Buell, R. P. Dickinson, D. A. Kozlowski, N. J. Marechal, and T. J. Wright, Appl. Opt. **44,** 7621 (2005).
3. Y. Zhou, N. Xu, Z. Luan, A. Yan, L. Wang, J. Sun, and L. Liu, Acta Opt. Sin. **29,** 2030 (2009).
4. L. Liu, Y. Zhou, Y. Zhi, J. Sun, Y. Wu, Z. Luan, A. Yan, L. Wang, E. Dai, and W. Lu, Acta Opt. Sin. **37,** 0900112 (2011).
5. B. Krause, J. Buck, C. Ryan, D. Hwang, P. Kondratko, A. Malm, A. Gleason, and S. Ashby, in *Proceedings of OSA/CLEO/QELS* PDPB7 (2011).
6. L. Liu, Acta Opt. Sin. **32,** 0920002 (2012).
7. L. Liu, Appl. Opt. **52,** 579 (2013).
8. Z. Luan, J. Sun, Y. Zhi, Y. Zhou, L. Wang, and L. Liu, Acta Opt. Sin. **34,** 0710003 (2014).
9. Y. Zhou, L. Wang, Y. Zhi, Z. Luan, J. Sun, and L. Liu, Acta Opt. Sin. **29,** 3291 (2009).
10. L. Liu, Acta Opt. Sin. **34,** 0528001 (2014).
11. Q. Xu, Y. Zhou, J. Sun, Y. Zhi, X. Ma, Z. Sun, D. Lu, and L. Liu, Proc. SPIE **8877,** 88770K (2013).